Geochemistry, Geophysics, Geosystems®

RESEARCH ARTICLE
10.1029/2025GC012160

Mantle Flow and Anisotropy in Subduction Zones: Modeling and Clustering of Olivine Textures

Yijun Wang[1], **Ágnes Király**[1], **Clinton P. Conrad**[1], **and Valerie Maupin**[1]

[1]Center for Planetary Habitability (PHAB), University of Oslo, Oslo, Norway

Key Points:

- Time-series clustering is useful for quantitatively characterizing rock texture heterogeneities within geodynamic model results
- Due to their greater deformation, retreating trenches exhibit stronger viscous and seismic anisotropy than stationary trenches
- For the most deformed regions, anisotropic viscosity tends to make rock textures even more point-like, thus enhancing seismic anisotropy

Supporting Information:

Supporting Information may be found in the online version of this article.

Correspondence to:

Y. Wang,
yijun0509wang@gmail.com

Citation:

Wang, Y., Király, Á., Conrad, C. P., & Maupin, V. (2025). Mantle flow and anisotropy in subduction zones: Modeling and clustering of olivine textures. *Geochemistry, Geophysics, Geosystems*, *26*, e2025GC012160. https://doi.org/10.1029/2025GC012160

Received 9 JAN 2025
Accepted 19 JUN 2025

Author Contributions:

Conceptualization: Yijun Wang
Data curation: Yijun Wang
Formal analysis: Yijun Wang
Investigation: Yijun Wang
Methodology: Yijun Wang
Resources: Yijun Wang
Software: Yijun Wang
Validation: Yijun Wang
Visualization: Yijun Wang
Writing – original draft: Yijun Wang
Writing – review & editing: Yijun Wang

Abstract

The mantle near Earth's subduction zones endures intense deformation that generates anisotropic rock textures. These textures can be observed seismically and modeled geodynamically, but the complexity of this deformation makes analyses of these textures difficult. In this study, we apply time-series clustering analysis to tracers within subduction models, allowing for the identification of regions in the subduction zone with common deformation histories and olivine crystallographic-preferred orientation development. We compare olivine texture evolution predicted using different methods in both retreating and stationary-trench settings. Our results reveal distinct variations in olivine texture, indicating that both seismic and viscous anisotropy can exhibit substantial heterogeneity within the mantle wedge, sub-slab, and subducting plate regions. For retreating trenches, olivine textures are strongest in the mid-depth mantle wedge region about 200 km away from the trench between 100 and 300 km depth. Our study shows that trench-normal olivine *a*-axis orientations dominate in the center of subduction zones. Toroidal flow around slab edges generates a mix of trench-normal, trench-parallel, and oblique fast seismic directions. Textures and anisotropy are stronger for the retreating trench model than for the stationary trench model since more deformation has been accumulated due to trench motion. These findings provide insights for interpreting seismic anisotropy in subduction zones and highlight the importance of considering texture heterogeneity, as characterized by clustering algorithms, when analyzing both geodynamic models and seismic observations of subduction zones.

Plain Language Summary

In subduction zones where one tectonic plate sinks beneath another, rocks in the mantle deform with the flow generated by the down-going slab. They develop textures that affect how seismic waves travel through them. These patterns can be detected using seismic data, but interpreting them is challenging due to the complexity of the deformation. In this study, we simulate subduction with two different styles: one where the trench (the boundary between the down-going plate and the upper plate on Earth's surface) moves backward (retreats), and one where it stays put. By tracking how rocks deform over time and applying a machine-learning method called time-series clustering, we were able to group regions of the model that share similar evolutions in deformation histories and rock textures. These patterns, in turn, influence both seismic wave speeds and how the mantle flows. We found that the type of subduction matters: retreating trenches cause stronger and more varied rock textures than stationary ones, especially in the upper mantle between 100 and 300 km depth. Most textures align with the direction the slab is sinking (trench-normal), but around the edges of the slab, swirling (toroidal) flow causes more complex patterns.

1. Introduction

The subduction process, where the cold and dense oceanic lithosphere sinks into the mantle, is the primary driver of plate tectonics and mantle flow. Subduction zones are also critical geological settings at the Earth's surface, associated with natural hazards such as earthquakes and volcanic eruptions. Understanding the interaction between the sinking slab and the surrounding mantle is crucial for comprehending the dynamics of subduction (e.g., Crameri et al., 2019; Faccenna et al., 2014; Király et al., 2017; Schellart & Moresi, 2013; Schellart et al., 2007). As a slab sinks into the mantle, patterns of flow that are produced include poloidal flow, which is vertical flow induced by the sinking motion of the slab (also referred to as corner flow in the mantle wedge and entrained flow beneath the slab), and toroidal flow, which is horizontal flow around the lateral edges of the slab. Such flows have been observed in laboratory studies (e.g., Duarte et al., 2013; Funiciello et al., 2003, 2006; Guillaume et al., 2021; Strak & Schellart, 2014) and numerical models (e.g., Faccenda & Capitanio, 2012; Jadamec & Billen, 2010; Király et al., 2017; Piromallo et al., 2006). The indirect observation of rock textures associated with mantle flow, in the form of seismic anisotropy, has long been recognized as a way to understand the dynamics of subduction (e.g., Becker et al., 2006; Long, 2013; Long & Wirth, 2013; Lynner & Beck, 2020; Lynner & Long, 2014;

Walpole et al., 2017). To adequately interpret flow patterns in the vicinity of subduction, however, it is necessary to link an observable indicator of the flow, such as seismic anisotropy, to the flow fields associated with subduction. Making this link requires a variety of constraints and modeling tools related to rock texture development within the flow fields of subduction systems. A deeper understanding of these rock textures and the mantle flow fields associated with them can provide more insight into the mantle dynamics of subduction zones.

Seismic anisotropy observations have provided a powerful constraint on mantle dynamics in subduction zones due to the direct association between deformation processes and seismic anisotropy (Long & Becker, 2010; Skemer & Hansen, 2016). Upper mantle rocks respond to deformation by developing a crystallographic-preferred orientation (CPO). The CPO of the most abundant mineral in the upper mantle, olivine, exhibits directional-dependent seismic wave speeds, which can be observed as seismic anisotropy (Karato et al., 2008). From the relationship between the applied deformation and seismic anisotropy, we can infer patterns of mantle flow (Ribe, 1989). For example, toroidal and poloidal flows have been inferred from seismic observations made near different subducting plates (Civello & Margheriti, 2004; Peng et al., 2021; Zhu et al., 2020). More generally, seismic anisotropy (e.g., SKS splitting) observations collected near subduction zones tend to show trench-parallel flow directions for the mantle beneath the slab (the sub-slab region) and a mix of trench-parallel and trench-normal flow directions for the mantle above the slab (the mantle wedge region) (Baccheschi et al., 2024; Long, 2013; MacDougall et al., 2012; Rappisi et al., 2022).

Apart from seismic anisotropy, olivine CPO also generates mechanical anisotropy in its viscous properties. Olivine deformation experiments by Hansen et al. (2012), Hansen, Warren, et al. (2016) and Hansen, Conrad, et al. (2016) demonstrated that olivine textures developed in extension led to strengthening for subsequent deformations applied in torsion across the original texture. The same is true in reverse, with texture developed in torsion leading to strengthening for subsequent extension across the developed texture. Hansen, Warren, et al. (2016) and Hansen, Conrad, et al. (2016) provided parameters that characterize this viscous anisotropy of olivine for use in geodynamic models (e.g., Király et al., 2020).

Recently, Wang et al. (2024) investigated the potential influence of anisotropic viscosity (AV) for textures in different regions of a subduction zone, focusing on two individual tracers in the mantle wedge and sub-slab regions. They computed olivine textures as a post-processing step using D-Rex (Fraters & Billen, 2021; Kaminski et al., 2004), the modified director method (MDM from Hansen, Warren, et al., 2016; Hansen, Conrad, et al., 2016), and MDM with the implementation of AV (MDM + AV from Wang et al. (2024)). Besides the difference that D-Rex produces more point-like textures while MDM generates more girdle-like textures, their results also revealed significant differences between CPO formed with and without AV for the two tracers on opposite sides of the slab. They also found that AV impacts tracers in the mantle wedge and sub-slab regions differently. These differences may complicate the use of seismic anisotropy to infer mantle flow patterns, highlighting the need for a more comprehensive investigation of the whole subduction zone, including the role of AV.

Previous studies that tracked rock texture development around subduction zones (e.g., Di Leo et al., 2014; Faccenda, 2014; Fraters & Billen, 2021) have identified significant spatial and temporal variability among the textures predicted on both sides of the slab. Such variations in olivine textures result from the distinct subduction-induced flow patterns (Magni et al., 2024) related to the time-dependent and 3D nature of subduction (Faccenda & Capitanio, 2012, 2013). Thus, the complexities of rock textures around subduction zones may be indicative of the time-integrated deformation history of subduction and subduction styles (e.g., retreating or stationary). Seismic anisotropy has been utilized to infer textures formed in the mantle (VanderBeek & Faccenda, 2021); however, due to the inherent complexity of subduction dynamics, rock texture formation, and their interlinked connection, such interpretation is not straightforward. Furthermore, under different stress and water content, the seismic fast direction might align differently relative to the flow direction depending on the type of olivine fabric formed (Jung & Karato, 2001), further complicating the interpretation of seismic anisotropy observations. A method to comprehensively analyze texture evolution within subduction models is needed, especially one that characterizes the complexity of the textures that form within the flow generated by the slab. Since CPO-induced AV is also dependent on the time evolution of deformation, such an analysis would benefit the understanding of AV in subduction systems as well.

In this study, we analyze the evolution through time of two 3D subduction models during their free-fall and interaction with the transition zone: one with a retreating trench and the other with a relatively stationary trench

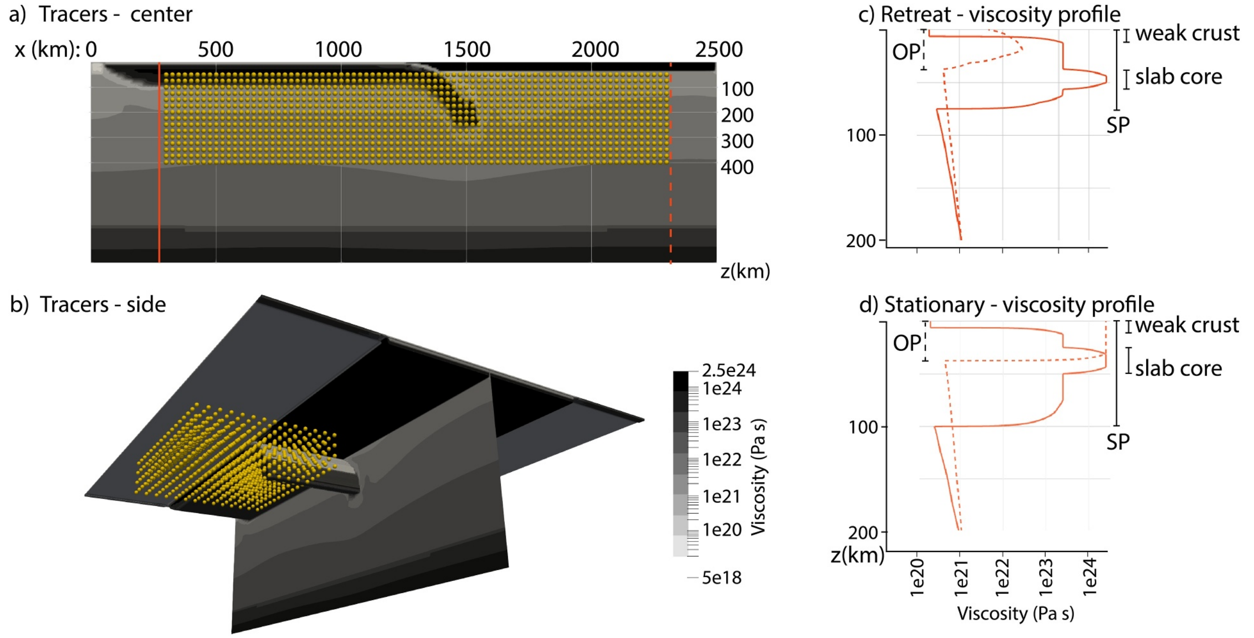

Figure 1. Initial setup of the subduction model showing viscosity as background (colors) and the tracers on the cross-section along the *x*-direction in the middle of the model (a) and around the edge of the slab (b). On the right side, we show two viscosity profiles from the subduction model with a retreating trench (panel c) and a stationary trench (panel d). The viscosity profiles are taken within the subducting plate (SP) and the overriding plate (OP) and away from the subducting slab ranging from 0 to 200 km depth (see the solid and dashed line on panel (a), respectively).

(Funiciello et al., 2006) (Figure 1). We computed the principal stresses, accumulated strain, olivine CPO, and CPO-induced AV for tracers placed within the model in the mantle regions in and around the slab. To characterize the complexity of the resulting rock textures, we group them according to the deformation history and CPO evolution using time-dependent clustering analysis (Kanungo et al., 2002; Warren Liao, 2005). Time-series clustering analysis is an unsupervised learning method used to group large data sets based on the similarity between time-series data. We identify tracers within a subduction system that share a similar evolution history and a similar path toward the formation of anisotropic rock fabrics. Classifying the textures for the different regions of the subduction zone helps us to understand patterns of anisotropic fabrics around the slab and offers insight into the interpretation of observations of seismic anisotropy.

2. Methods

2.1. Model Setups

We run two subduction models with the same free-slip boundary conditions and rheology parameters but different initial geometries and temperatures to facilitate a retreating trench and a relatively stationary trench. Our models were built using the geodynamic modeling framework ASPECT (Bangerth et al., 2022; Fraters & Billen, 2021; Heister et al., 2017; Kronbichler et al., 2012), following the rheology and boundary conditions from Behr et al. (2022) and Turino and Holt (2024). The model space spans 2,500, 2,000, and 800 km in *x*-, *y*-, and *z*-directions (length, lateral width, and depth, respectively) (Figures 1a and 1b). The subducting plate is located 500 km away from both lateral sides of the box and spans 1,000 km in the center. Since the trench lies along the direction of the *y*-axis, we describe the orientations of olivine textures parallel to the *y*-axis as trench-parallel (TP) and perpendicular to the *y*-axis as trench-normal (TN). The models consist of a 10-km-thick weak crust that decouples the subducting plate from the overriding plate, a strong slab core (10 km or 15 km), lithosphere (80 km or 100 km), an overriding plate (30 km or 40 km), a weak box at the end of the subducting plate functioning as a ridge-like thermal structure, and background mantle material (Figure 1c). We use a stronger and thicker overriding plate and a steeper-dipping subducting plate that extends deeper into the mantle to make a stationary-trench model (e.g., trenches in the Sunda subduction system with a relatively slow trench velocity) in contrast to the Chilean-type retreating-trench model (Gea et al., 2024; Royden & Husson, 2006) (Figure 1d). There are no imposed velocity boundary conditions, and the model is completely dynamic. We let the system evolve selfconsistently until 40 Myr. By the end of the retreating-trench model, about 240 km of the slab has been subducted coupled with 400 km trench retreat; for the stationary-trench model, about 300 km of the slab has been subducted.

We place tracers in two different locations: both away from and close to the slab edge. One thousand two hundred fifteen tracers are placed on the cross-section cutting vertically across the plate at $y = 1{,}000$ km from $x = 200$–2,300 km and from a depth of 50 to 400 km with a resolution of 25 km to cover areas such as the mantle wedge above the slab and the sub-slab region (Figure 1a). In addition, 952 tracers were placed in a box next to the lateral edge of the slab from $x = 1{,}000$ to 1,800 km, $y = 50$ to 700 km, and $z = 100$ to 250 km with a resolution of 50 to track both the horizontal toroidal flow and the associated upwelling around the slab edge (Figure 1b). These tracers are advected with the flow field and thus effectively record evolution along flow lines. In ASPECT, we store properties on the tracers that describe the deformation history such as strain rate, stress, and velocity gradients for computations of olivine CPO and CPO-induced AV as a post-processing step (Wang et al., 2024).

2.2. Texture Prediction

We start the model with initial random orientations on the tracers. The texture evolution does not modify the deformations in the model, which is driven by gravitational force due to the temperature-dependent density. As a post-processing step, olivine textures are predicted using D-Rex (Kaminski et al., 2004), MDM (Hansen, Conrad, et al., 2016; Hansen, Warren, et al., 2016), or MDM + AV (Wang et al., 2024), the last of which includes the influence of anisotropic viscosity on texture development. D-Rex is a kinematic model that computes textures based on the initial textures and deformation history, taking into account dynamic recrystallization. MDM is a director-based model with improved computational efficiency. Finally, MDM + AV computes the viscosity tensor in the CPO-reference frame, which is rotated into the model reference frame to calculate the resulting deformations. For MDM and MDM + AV, we incorporate a pseudo-phase transition in predicting the olivine fabric. The texture is reset to random whenever a tracer crosses 410 km depth and the anisotropic viscosity tensor is fixed as the identity tensor while the tracer stays below 410 km.

The olivine texture can be characterized by its strength (M-index from Skemer et al. (2005)), shape scores (a-axis pointiness and girdle-ness scores from Vollmer (1990), referred to as P and G scores later), and the mean orientation of the olivine a-axis. The effective anisotropic viscosity ($\eta_{\text{effective\_AV}} = \sigma / \dot{\varepsilon}_{\text{AV}}$) is computed using the second invariant of the stress tensor (σ) from ASPECT and the second invariant of the strain rate tensor ($\dot{\varepsilon}_{\text{AV}}$) predicted under AV as in Wang et al. (2024), who describe the AV tensor using Hill's coefficients (Hill, 1948; Signorelli et al., 2021). The change in viscosity under deformation with and without viscous anisotropy is assessed with the AV-to-IV ratio ($\eta_{\text{effective}_{\text{AV}}} / \eta_{\text{effective}_{\text{IV}}}$), where $\eta_{\text{effective}_{\text{IV}}} = \sigma / \dot{\varepsilon}_{\text{IV}}$, and $\dot{\varepsilon}_{\text{IV}}$ is the second invariant of the predicted strain rate tensor assuming a uniform texture that represents isotropic viscosity. We also computed the principal stresses on the tracers from the deviatoric stress tensor derived from the subduction model in ASPECT as an aid to understanding the relationship between the evolution of AV and olivine texture. All of these quantities are recorded as a function of time as the tracers move through the subduction zone, to be used later by the clustering algorithm.

2.3. Clustering Analysis

Time-series clustering is a method for partitioning a time-series data set into a certain number of clusters based on criteria for assessing the distance or similarity between the data points. This method is specifically suitable for this study since olivine CPO and CPO-induced AV are dependent on deformation histories and the amount of information to analyze is large. We apply time-series clustering to find regions within a subduction system that share a similar evolution pattern for olivine CPO, CPO-induced AV, and mantle flow. By tracking the tracers over time, we gather time-series data including tracer paths, texture parameters, and AV. Specifically, we use the time-series k-means method (Kanungo et al., 2002), an unsupervised partition-based clustering algorithm in which observations are categorized into clusters with the nearest mean. The basic idea behind k-means clustering is to partition a data set into k clusters by iteratively assigning data points to the cluster whose centroid is closest. TimeSeriesKMeans extends this concept to time-series data, considering both the spatial proximity of data points and their temporal evolution (Warren Liao, 2005). The data matrix that goes into the clustering algorithm is a three-dimensional $n*p*q$ (number of tracers * attributes * time steps) matrix $T = \{t_1, t_2, \ldots, t_n\}$, where t_i represents one observation as a $p * q$ matrix containing time-series data of all p attributes through all q time steps for one tracer. We aim to partition the n observations into a total of k clusters ($k < n$), that is, $C = \{C_1, C_2, \ldots, C_k\}$, by minimizing the inertia score, given as:

Inertia $= \sum_{j=1}^{k} \mathrm{DTW}(t_i - C_j)$, where t_i belongs to the cluster C_j, and $\mathrm{DTW}(t_i - C_j)$, denotes the dynamic time warping distance between t_i and the center of cluster C_j, which is a measure of similarity between time-series data and takes into consideration time shifts, stretches, and compressions.

In order to study the relationship between CPO and CPO-induced AV, we used the MDM + AV textures to build our data matrix, as they incorporate the effect of AV. We conducted two separate cluster analyses for the tracers placed away from and close to the slab edge to look at poloidal- and toroidal-dominated flows, respectively, for each subduction model. In one model for the tracers away from the slab edge, for example, we obtain one data matrix of tracer locations as a function of time with a dimension of 1,215 tracers * 40 timesteps * 3 coordinates along the x-, y- and z-axes, as one data set for clustering. From the post-processing calculation of texture, we obtain another data matrix of tracer scores that describe olivine texture (P and G scores, M-index, J-index and mean a-axis orientation as sins and cosines of both the horizontal and vertical orientations), CPO-induced viscous anisotropy (AV/IV), and deformation state (principal stresses, and accumulated strain), its dimensions being 1,215 tracers * 40 timesteps * 13 attributes. We combine the two data sets (three coordinate attributes and 13 texture-related attributes) into a 1,215*40*16 matrix and perform principal component analyses to find the relative importance of these attributes for explaining the evolution pattern. With the most important attributes (a threshold of 0.33), we apply time-series clustering analysis to identify potential patterns of evolutions in tracer paths, CPO, and AV in different regions of subduction systems. The attributes are also normalized to have the same mean and standard deviation so that all attributes have the same weight in calculating the relative importance and the inertia score. In the Python-based TimeSeriesKMeans package, K-means utilizes an iterative procedure with the following steps to derive the final category for each time-series candidate:

1. Initialize k cluster centroids C_1, C_2, … C_k, arbitrarily.
2. Assign each observation t_i to cluster C_j so that the total distance between t_i and its cluster center C_j is minimal.
3. Update each cluster center C_j with the assignments of observation t_i into C_j in step 2.
4. Repeat steps 2 and 3 until convergence (inertia between two consecutive iterations changes no more than a threshold).

We experimented with different k values and the total number of clusters, and employed the inertia score (Hartigan & Wong, 1979), silhouette score (Rousseeuw, 1987), and Davies-Boudin Index (Davies & Bouldin, 1979) to assess the quality of clustering results (Figure S1 in Supporting Information S1). Silhouette Score quantifies how similar an object is to its cluster compared to other clusters. The formula is given by

$$\text{Silhouette Score} = \frac{1}{n}\sum_{i=1}^{n}\frac{b-a}{\max(a,b)},$$

where a is the distance of one observation from all other observations in the same cluster, and b is the distance of this observation from all observations in the next-closest cluster. A higher silhouette score suggests that the clusters are well-defined and distinct from each other. Davies-Bouldin Index measures the within-cluster compactness and the separation between clusters. It is defined as

$$\text{Davies} - \text{Bouldin Index} = \frac{1}{K}\sum_{i=1}^{K}\max_{j\neq i}\left(\frac{S_i + S_j}{d(c_i, c_j)}\right),$$

where S_i and S_j are the average distance between each pair of observations from cluster i and cluster j, and $d(c_i, c_j)$ is the distance between cluster centroids c_i and c_j. Finding an optimal clustering result involves finding a value of k that simultaneously minimizes inertia, maximizes silhouette scores, and minimizes Davies-Bouldin index values. We also take into consideration realistic factors, for example, that there should be at least three clusters representing material above, within, and below the slab. The upper bound is limited to ensure that the resulting clusters remain meaningful and interpretable. We pick $k = 14$ for tracers in the center of the subduction zone. Following similar criteria, we pick $k = 10$ and 11 for tracers near the slab edge for the subduction model with a

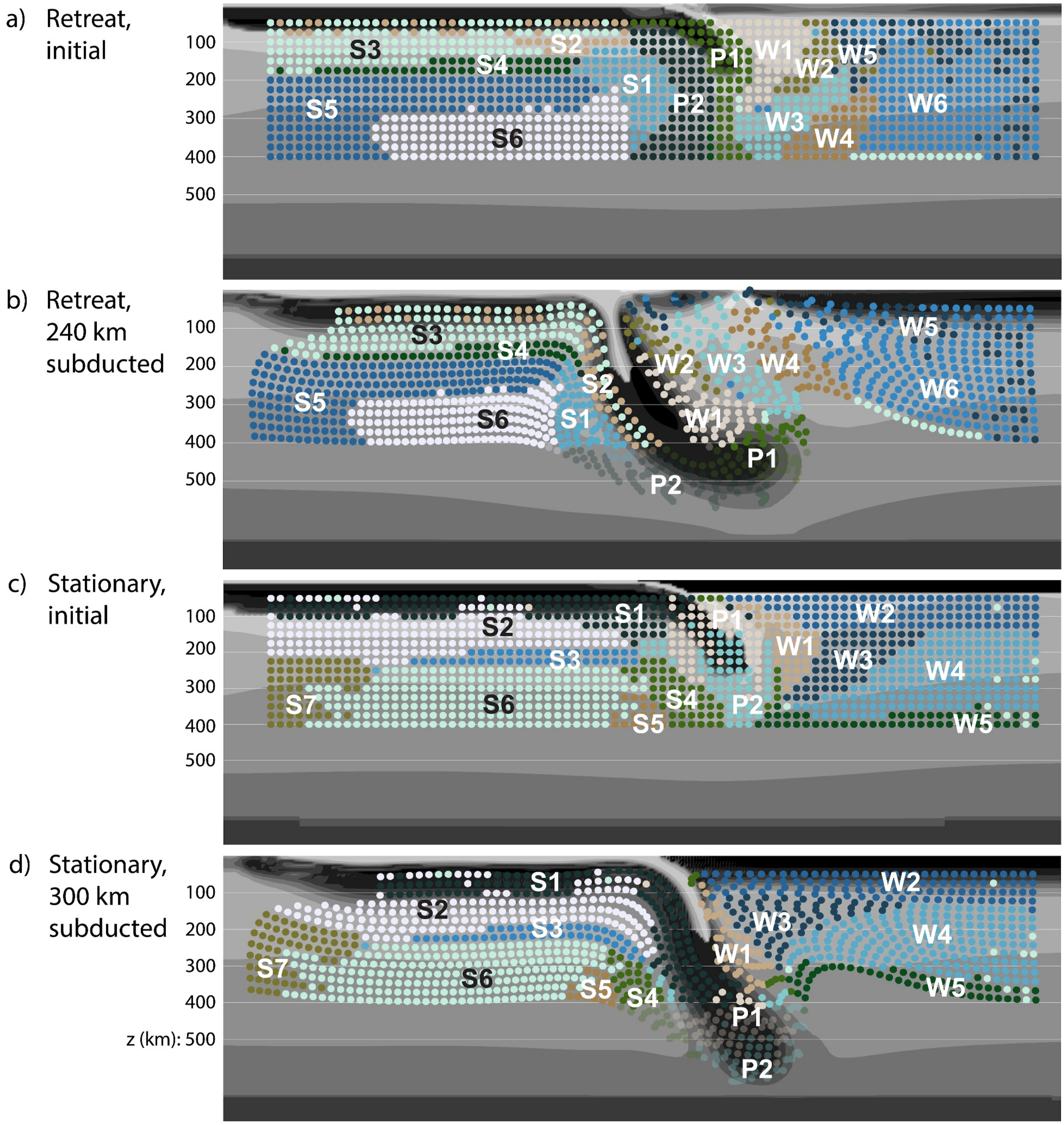

Figure 2. Tracers on the cross-section along the *x*-direction in the middle of the subduction model with a retreating trench (a and b) and a stationary trench (c and d), colored by cluster assignment. The names of the clusters are labeled on top of the tracers.

retreating trench and a stationary trench, respectively (see Figure S1 in Supporting Information S1 for details on selecting *k*).

3. Results

Cluster assignments are visualized in Figures 2 and 5, and variations in the temporal evolution of attributes across clusters are evident in the cluster means (Figures 3–6). We first present the clustering results for tracers in the center of the subduction model (Section 3.1; Figures 2–4) and then present the results for tracers at the slab edge (Section 3.2; Figures 5 and 6). Feature importance analysis reveals that the evolution of *x*, *y*, and *z* coordinates and

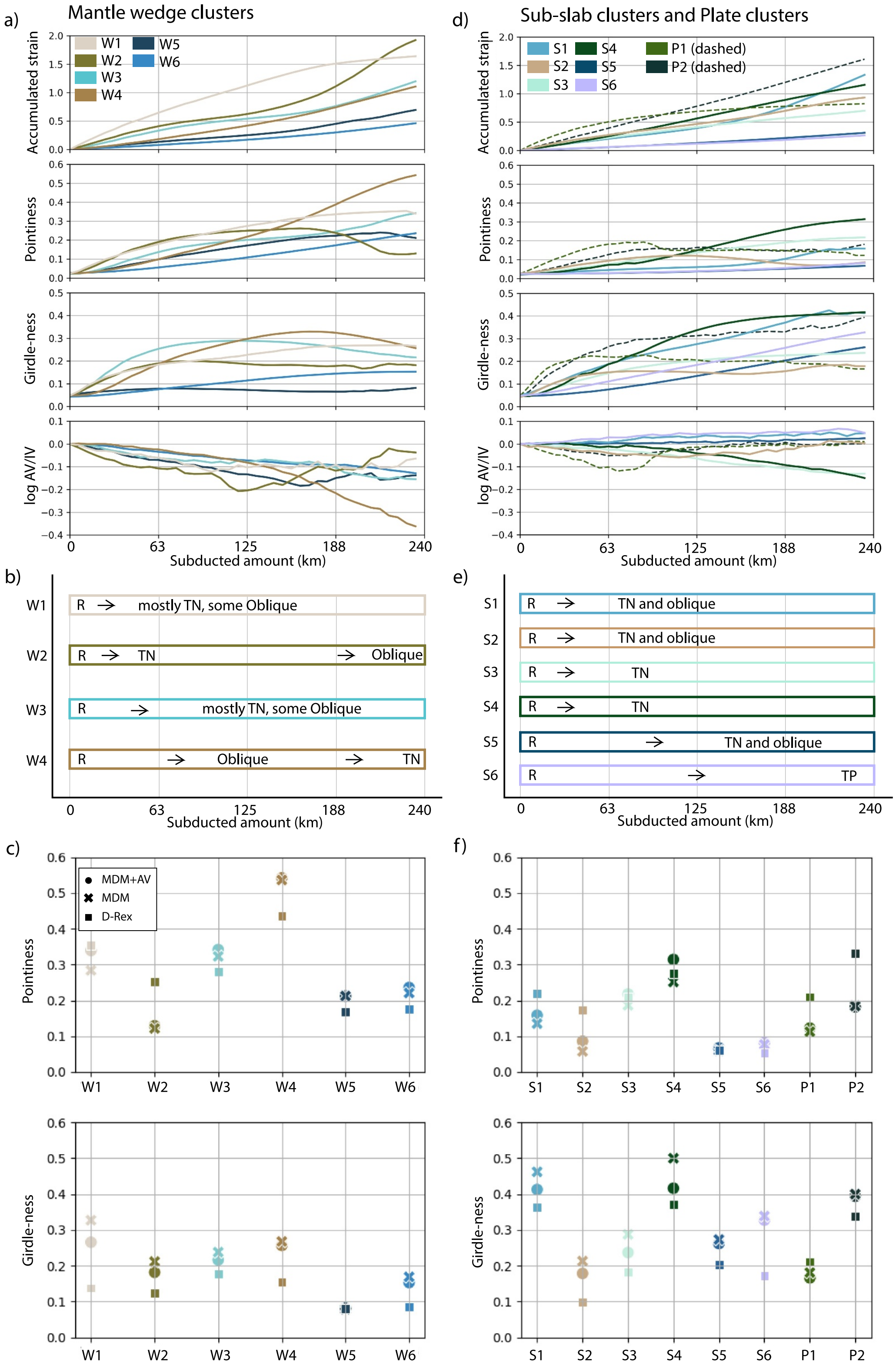
a)
Mantle wedge clusters
W1
W2
W3
W4
W5
W6
Accumulated strain
Pointiness
Girdle-ness
log AV/IV
Subducted amount (km)
0
63
125
188
240
b)
R → mostly TN, some Oblique
R → TN → Oblique
R → mostly TN, some Oblique
R → Oblique → TN
c)
MDM+AV
MDM
D-Rex
d)
Sub-slab clusters and Plate clusters
S1
S2
S3
S4
S5
S6
P1 (dashed)
P2 (dashed)
e)
R → TN and oblique
R → TN and oblique
R → TN
R → TN
R → TN and oblique
R → TP
f)
P1
P2

Figure 3.

the P and G scores are the attributes that contribute most significantly. Apart from these, with a threshold of 0.33, at least one attribute that describes the texture strength, orientation, and/or principal stresses is included (Figure S2 in Supporting Information S1). We show that the mean evolution of accumulated strain, P-score, G-score, and AV/IV ratio, which are mostly related to the development of AV, allows us to analyze the relationship of AV to deformation histories and olivine textures (Wang et al., 2024). As shown in Figure 2, tracers are clustered into small groups within larger areas for both subduction models with a retreating or stationary trench. We name these clusters with a letter related to their geographical positions with respect to the slab: mantle wedge (cluster group W), sub-slab (cluster group S), and subducting plate (cluster group P). Our categorization of tracers using time-series clustering analysis reveals the different types of textures that form in the mantle regions that surround a subduction zone. In particular, tracers that have been through the phase transition at 410 km depth are clustered together. While viscous anisotropy has been erased for these clusters, we can still infer the relationship between CPO and CPO-induced anisotropy for other clusters that are not significantly affected by phase transition.

3.1. Tracers Affected by the Poloidal Flow

In Figure 2, we show the optimal cluster assignment with $k = 14$ for tracers in the center of the subduction models at its initial and end stages. Most tracers within each cluster are not spread throughout the model but are located close to each other and limited to specific regions. However, clustering for the shallow region below the subducting plate and for the mantle wedge region far from the trench is poorly defined, as shown by the clusters mixed together (e.g., W5 with W6, S2 with S3 in the retreating-trench model). Therefore, we focus on the clusters close to the slab, which provide more useful information.

3.1.1. Subduction With a Retreating Trench

In the subduction model with a retreating trench, approximately 240 km of the slab has been subducted, excluding the initial slab length, reaching about 500 km depth and curling upwards, while the trench retreated about 200 km (Figure 2b).

There are six clusters above the slab in group W. Clusters W1–W4 are located from small to larger distances to the slab, respectively (Figure 2a). They accommodated larger deformations and therefore exhibit better within-cluster compactness and representative mean values with a smaller spread than W5 and W6 located farther away from the slab. Tracers in W1 to W4 shift from random to trench-normal (TN) orientations, with alignment taking place earlier in shallower clusters (W1 and W2 after 60 km, W3 after 100 km, and W4 after 200 km of slab subduction as shown in Figure 3b). This alignment occurs when the P-scores approach their peaks, after the initial development of a girdled texture stops (W1) or starts to disappear (W2, W3, and W4) (Figures 3a and 3b). Subsequently, the shallower clusters (W2) develop weaker textures (decreasing P-score) in different trench-oblique orientations after they are aligned to TN orientations, while W3 and W4 have just reached TN alignment at the end of the model (Figures 3a and 3b). Across all mantle wedge clusters, AV induces mantle weakening when textures align with the trench-normal direction, and the maximum weakening occurs when the P-score reaches its peak and the G-score is not growing (Figure 3a). The most weakening (AV being about 40% of IV) occurs in cluster W4, which is about 200 km away from the slab and moves from about 300 km depth to above 300 km.

Tracers in clusters P1 and P2, located in the slab and beneath the slab tip, respectively, develop similar textures to group W clusters. They mostly include the tracers that have been in the MTZ as the slab subducts. As a result, their textures are erased as soon as the tracers enter the mantle transition zone (MTZ), and the anisotropic viscosity is also reset to isotropy. This resetting is not fully reflected in the mean P and G scores because as tracers gradually move into the MTZ and the drop in their P and G scores, other tracers in the same cluster are increasing their P and G scores, resulting in a net slow change of P and G. However, the mean AV/IV ratio evolutions of both clusters show anisotropic weakening in the early stage corresponding to the development of textures above 410 km, and then a return to isotropic after the majority of the cluster resides in the MTZ.

Figure 3. Summary of attributes for the different clusters away from the slab edge in the subduction model with a retreating trench (Figures 2a and 2b). On the left side, for group W clusters, we show the evolution of the mean values for different texture attributes against the amount of slab subducted including the accumulated strain, pointiness (P-score), girdle-ness (G-score), and AV/IV ratio (panel a), and the olivine *a*-axis orientations denoted by R (random orientations), TP (trench-parallel) and TN (trench-normal) (panel b). We also plot the P-score and G-scores at the end of the model (Figure 2b) predicted by MDM + AV, MDM, and D-Rex in (c). The same attributes are shown on the right for groups S and P clusters in panels (d)–(f). The colors correspond to the cluster assignment as shown in Figures 2a and 2b.

10.1029/2025GC012160

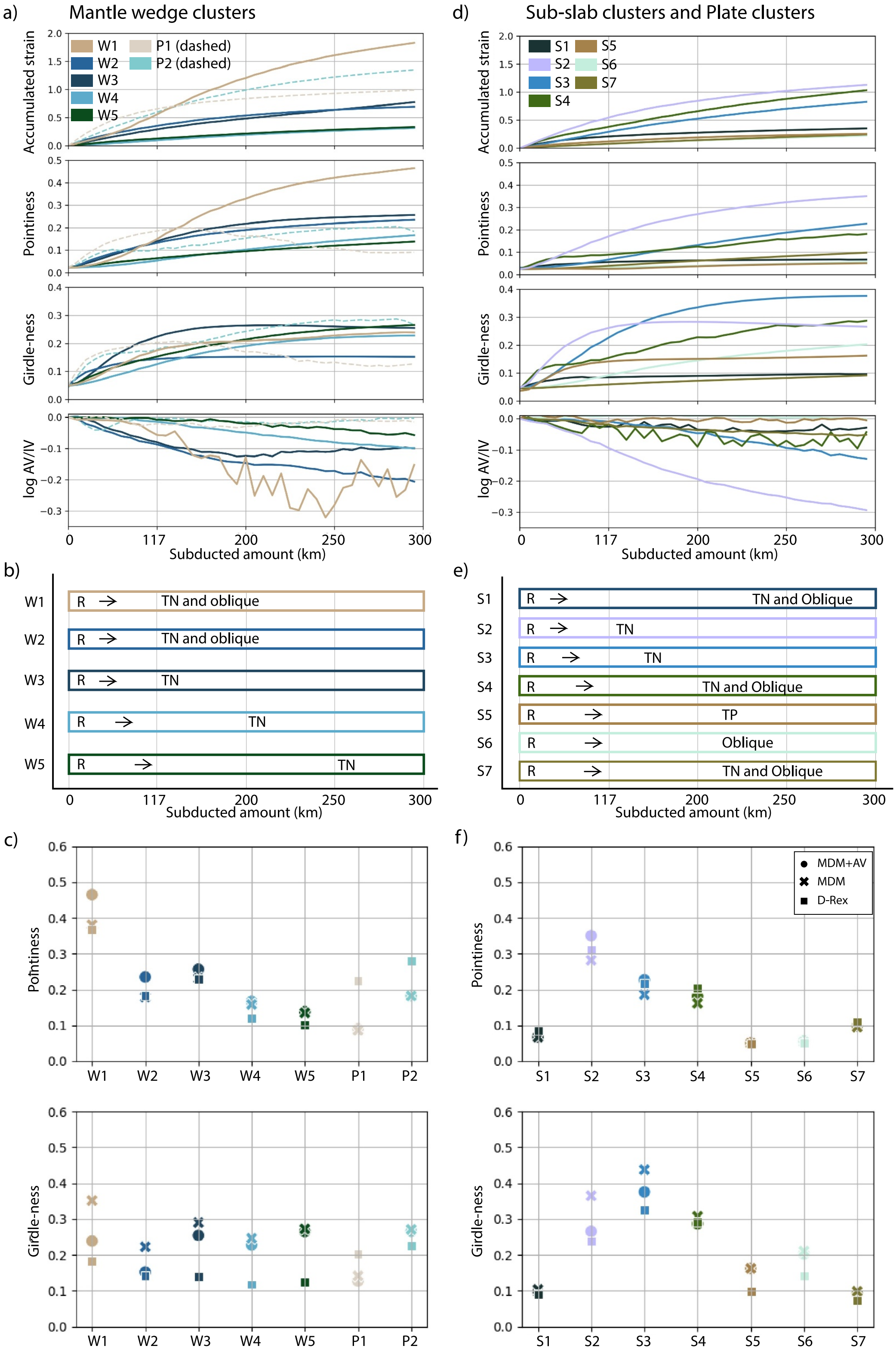

Figure 4. The same as Figure 3 for the subduction model with a stationary trench. The colors correspond to the cluster assignment as shown in Figures 2c and 2d.

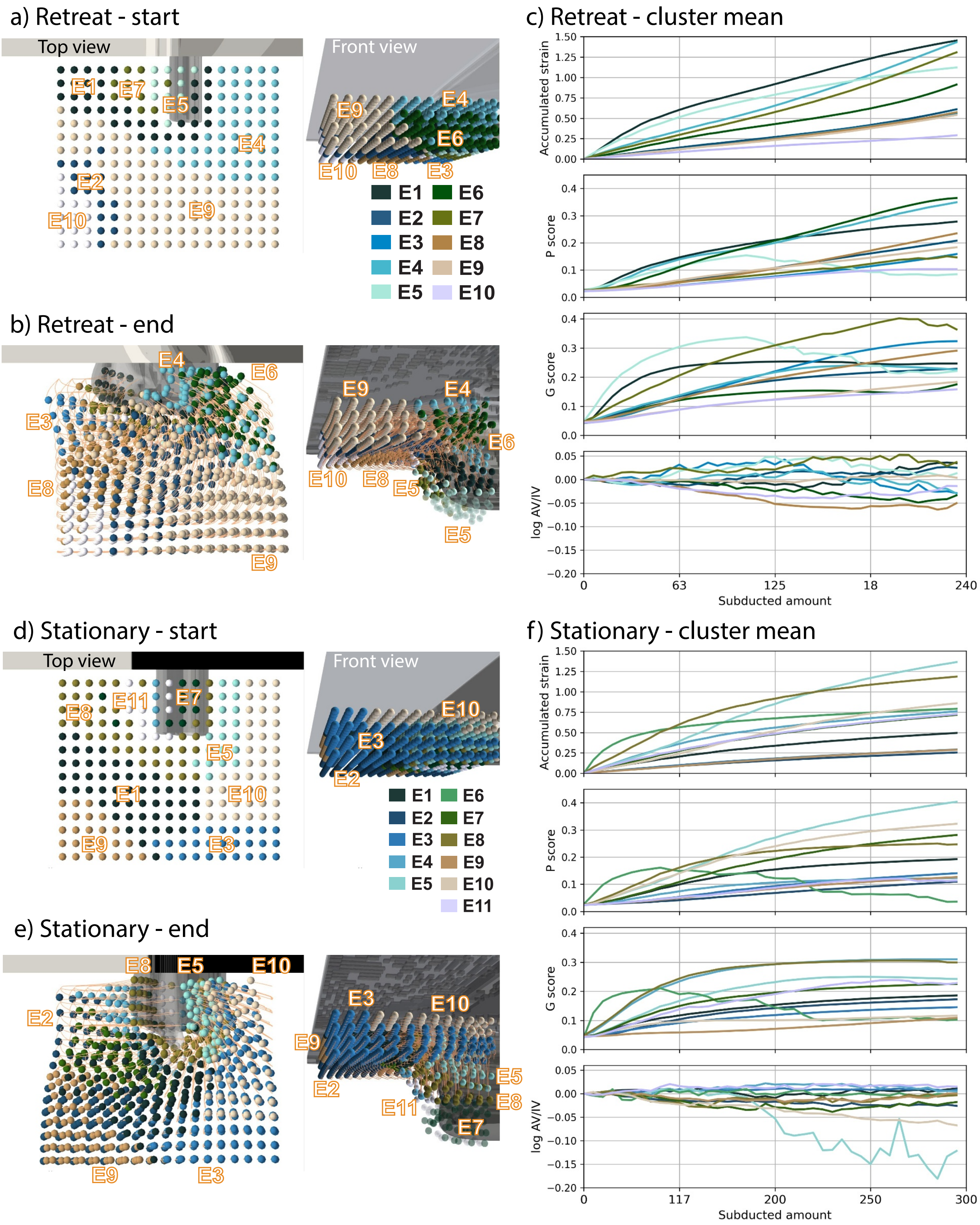

Figure 5. Clustering results at the slab edge for the subduction model with a retreating trench at (a) the initial stage and (b) the end of the model. The evolution of the mean values for attributes as a function of the amount of slab subducted is shown in panel (c), which includes the accumulated strain, P-score, G-score, and AV/IV ratio (as for Figure 3a). The same for the subduction model with a stationary trench is shown in panels (d)–(f). Colors in (c) and (f) correspond to those of the labeled clusters in (a) and (d), respectively.

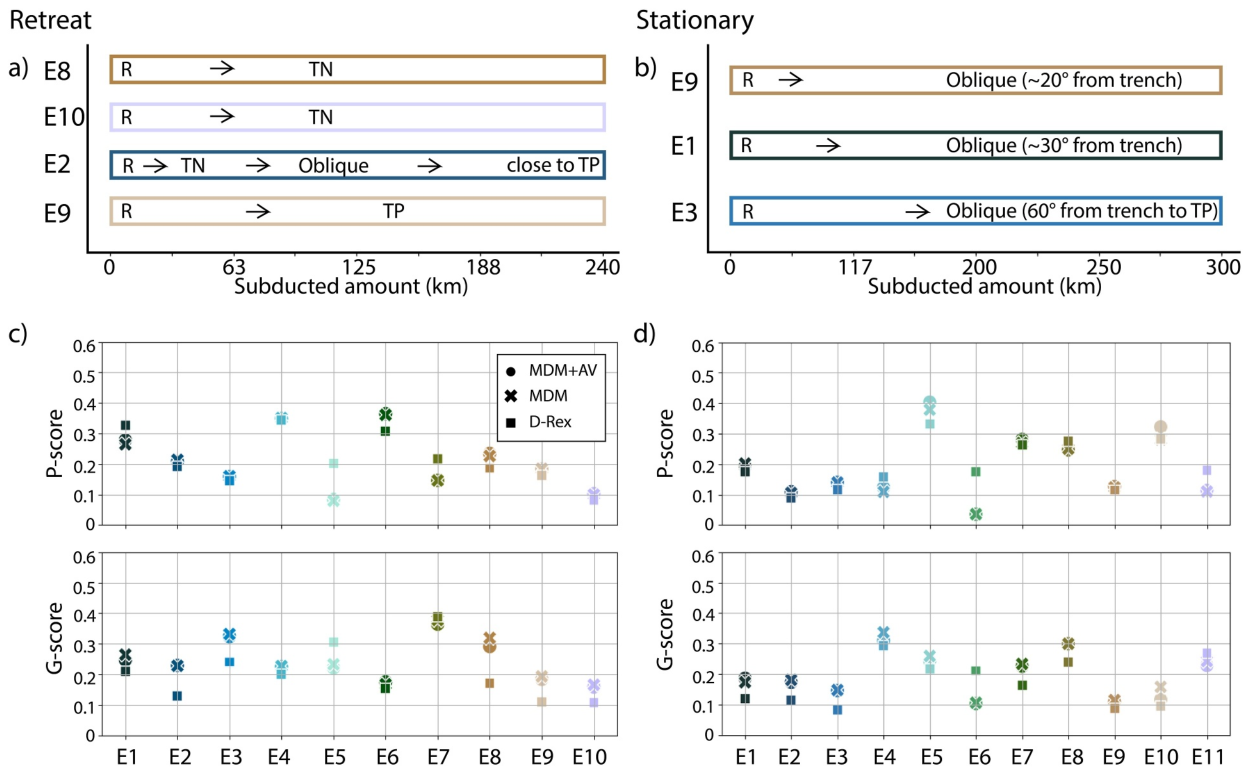

Figure 6. Summary of attributes for the different clusters close to the slab edge. For tracers in the subduction model with a retreating trench, trends in the evolution of the mean olivine *a*-axis orientations are shown as a function of the amount of slab subducted (a), while the P-score and G-score at the end of the model are shown (c), as predicted by MDM + AV, MDM, and D-Rex (symbols). The same analysis is shown on the right for the subduction model with a stationary trench in panels (b) and (d). The colors correspond to the cluster assignment as shown in Figure 5.

Clusters S1–S4, situated closely beneath the slab, follow texture evolutions similar to group W clusters, developing a weak TN orientation. Clusters S5 and S6, located farthest behind the slab, undergo the least movement and share a similar evolution history in their accumulated strain, P-score, and G-score. They both exhibit girdled textures while S6 captures the slightly stronger trench-parallel (TP) orientations surrounded by weak trench-normal orientations from S5. Here, only the most deformed clusters (S3 and S4) experience a weakening of AV to about 75% of IV (Figure 3d).

The differences between textures predicted by MDM + AV, MDM, and D-Rex at the end of the model also vary among the clusters (Figures 3c and 3f). In general, D-Rex tends to predict more point-like textures, while the MDM textures are more girdle-like. As the deformation accumulates, the difference between the P-scores of D-Rex and MDM + AV grows larger. However, tracers that experience weakening in AV relative to IV exhibit MDM + AV textures that become more point-like, and catch up to the D-Rex P-score (W4, S3, and S4 in Figures 3c and 3f, see the data folder on Zenodo (Wang, 2025) for comparisons at other time steps).

3.1.2. Subduction With a Stationary Trench

In the stationary-trench model, about 300 km of the plate, excluding the initial slab length, has been subducted while the location of the trench remains fixed (Figures 2c and 2d). Consequently, fewer tracers are transported to the mantle wedge, resulting in less deformation on all tracers compared with the retreating-trench model.

Above the slab, tracers are categorized into five clusters. W1, located closest to the slab, experiences the largest deformations (accumulated strain > 1.5), which leads to the strongest texture (P-score > 0.4) (Figure 4a). Consequently, W1 is the most weakened cluster with AV weakened to around 60% of IV. As in the retreating-trench model, shallower clusters align to trench-normal orientations earlier than deeper clusters (W2 to W5 from shallow to deep in Figure 4b). Behind the slab, S2, S3, and S4 are located closer to the slab (Figure 2) and can be differentiated from the less-deformed clusters. Their textures shift from random to trench-normal directions, starting with the shallowest cluster S2 (Figure 4e). The other clusters do not have a well-developed texture. Still, a small region with weak TP orientations (S5) is differentiated from its surroundings.

Texture predictions differ slightly among D-Rex, MDM, and MDM + AV, and the variations are smaller than in the retreating trench model (Figures 4c and 4f). Less deformed clusters (S1, S5, S6, and S7) exhibit minimal differences among methods, while the most deformed clusters (W1 and S2) exhibit larger differences. Clusters W1 and S2 also show a significant impact of AV (low log AV/IV ratio from Figure 4c), and their MDM + AV P-scores at the end of the model are also larger than the D-Rex P-score (Figure 4f), as we found for the retreating-trench model.

3.2. Tracers Affected by the Toroidal Flow

Tracers affected by the toroidal flow near the lateral edge of the slab track mantle flow both on horizontal and vertical planes and thus, their paths are more complicated. For the retreating-trench model, tracers behind the slab initially have been transported to regions in front of the slab, whereas in the stationary-trench model, less horizontal motion is observed due to the less intensive mantle flow (Figure 5). As for tracers on the center cross-section in the subduction models, clustering analysis for tracers on the lateral edge of the slab successfully categorizes the tracers into smaller groups that share a similar texture evolution, and we show the clustering results with $k = 10$ and $k = 11$ for the subduction model with a retreating trench and a stationary trench, respectively (Figure 5). To differentiate them with tracers in the center of the subduction zones, we designate these as the E-group (edge) clusters (Figure 5).

In the retreating-trench model, most of the tracers experience a shift from initial random orientations to trench-oblique orientations in different directions during the model, following their path along the horizontal toroidal flow. Clusters initially located on the side of the slab (E8, E10, E2) demonstrate an alignment with the trench-normal orientations (Figure 6a). Cluster E2 rotates further from TN to oblique and then to almost TP orientations as the tracers move toward the front of the slab. Clusters located in front of the slab (e.g., E9) do not have an intermediate stage of trench-normal orientation during the texture evolution and are mostly oblique and trench-parallel. AV is not significantly weakened in any of these clusters.

Trench stationarity leads to less vigorous toroidal flow, resulting in a large difference in the behavior of tracers on the side of the slab compared to the model with a retreating trench. The clusters still represent a part of the 3D flow pattern around the edge of the slab, but the olivine a-axis orientations are mostly trench-oblique in different directions and they have not developed strong TN or TP orientations as we found for similar clusters in the retreating-trench model (Figure 6b).

In general, toroidal flow produces smaller differences between textures predicted by D-Rex, MDM, and MDM + AV than for tracers dominantly deformed by poloidal flow (Figure 6). Similarly, clusters that are most affected by AV (clusters E6 and E8 from Figure 6a and E5 and E10 from Figure 6b) have MDM + AV P-scores that are larger than or similar to D-Rex P-scores (Figure 6).

4. Discussion

Our results demonstrate the benefits of using time-series clustering to identify groups of tracers with common evolution histories in subduction models. We used tracer locations and attributes related to olivine texture and texture-induced AV for clustering. The clustering results reveal that the large regions we call the mantle wedge, sub-slab, or subducting plate can be subdivided into smaller regions where different and unique olivine fabrics develop, resulting in heterogeneity in the seismic and viscous anisotropy. Such heterogeneity should not be neglected when we compare different texture prediction methods, examine olivine texture development in subduction zones, and interpret seismic anisotropy observations.

4.1. Olivine Texture Predictions and Cluster Analysis

Vigorous mantle flow in subduction zones induces time-dependent and spatially varied deformation in the asthenosphere. Laboratory experiments have demonstrated that a complex deformation history can play a significant role in olivine CPO formation and thus may complicate possible interpretations of seismic anisotropy, especially in subduction zones (Boneh & Skemer, 2014). The incorporation of such texture development models into time-dependent geodynamic models of subduction provides an opportunity to understand how the deformation history of tracers affects the fabrics that form in the vicinity of the slab (Faccenda & Capitanio, 2012, 2013). Tracers advected with the mantle flow can be used to record the deformation history and subsequently model CPO formation with texture evolution models, such as D-REX (Faccenda & Capitanio, 2012; Fraters & Billen, 2021; Kaminski et al., 2004) or VPSC (Di Leo et al., 2014; Tommasi et al., 2000).

In this paper, we model texture evolution on tracers from subduction models using the D-REX method (based on Fraters and Billen (2021)), the MDM (Hansen, Conrad, et al., 2016; Hansen, Warren, et al., 2016) method, and the MDM + AV (Wang et al., 2024) method. The MDM + AV method considers the anisotropic viscous effect on the evolving texture without modifying the tracers' path in the subduction model (Wang et al., 2024). Whereas Wang et al. (2024) compared textures predicted by D-Rex, MDM, and MDM + AV on two tracers moving through the subduction zone, our study expands this comparison to multiple tracers spanning the whole subduction zone region. Our results show that, as in previous comparisons, D-Rex usually predicts a more point-like texture, while MDM predicts a more girdle-like texture (Hansen, Conrad, et al., 2016; Hansen, Warren, et al., 2016; Wang et al., 2024). For clusters that are significantly weakened by AV (e.g., W4, S3, and S4 from the retreating-trench model and W1, and S2 from the stationary-trench model at the final step), the pointiness scores of MDM + AV textures are as large as or greater than the pointiness scores of textures predicted by D-Rex. Including AV could promote a more point-like texture when the deformation occurs in the preferred orientation.

Since olivine CPO and CPO-induced AV are both dependent on deformation history, time-series clustering analysis helps to identify regions that share similar deformation histories, which leads to similar textures and viscous anisotropy. As a result, it is easier to analyze the relationship between textures and anisotropy using the clusters. As is evident for clusters W1, W2, W3, S3, and S4 from the retreating-trench model, maximum weakening of AV occurs when a strong point-like texture develops and is aligned to the shear direction (Figure 3). The same can be observed in the stationary-trench model for clusters W1, and S1 (Figure 4) and in both models for tracers near the edge of the slab (Figure 5). Concerning the amount of deformation and the strength of the texture (measured by the P-score here), overall weakening by AV is larger and more widespread for tracers near the center of the subduction model with a retreating trench (Figures 3c and 3f). On the other hand, due to the rapid change of horizontal flow direction (toroidal flow), tracers near the edge of the subduction model with a retreating trench experience less weakening (Figures 6c and 6d).

We find that texture predictions show predominantly trench-normal orientations of the olivine *a*-axis (fast seismic direction) away from the slab edges, except between 300 and 400 km depths in the sub-slab area (cluster S2). These orientations are also in good agreement with previous modeling results of retreating subduction models (Di Leo et al., 2014; Faccenda & Capitanio, 2012, 2013). Trench-parallel directions are rare in the model with a stationary trench. Rather, we find a strong trench-normal alignment concentrated within small areas close to the overriding and subducting plates, where viscous coupling between the moving lithospheric plates and the asthenosphere promotes strong deformations. The corresponding regions (S2) that generate such signals are conveniently identified with the clustering method.

Fraters and Billen (2021) observed trench-parallel CPO in the mantle wedge region, some hundred kilometers away from an advancing (rolling forward) slab. Such CPO has not been found in our models, likely because the stationary trench or retreating trenches in our models result in different dynamics compared to the advancing trenches of Fraters and Billen (2021). Close to the slab edges, toroidal mantle flow dominates the CPO *a*-axes direction, rotating between trench-normal and trench-parallel and back to trench-oblique. Faccenda and Capitanio (2012) showed that the further we go from the trench, the more dominant trench-parallel directions become. In our retreating model, this can be somewhat observed by the strongest and mostly trench-oblique directions occurring furthest from the trench (Figure 8), albeit in our model only the areas closest to the slab edge and the trench are covered with tracers. Because toroidal flow is absent in the stagnant-trench model, we only find sub-vertical orientations with weak P-scores caused by the sinking of the slab in this case.

4.2. Comparison With Seismic Anisotropy Observations

The clusters we identify help to classify seismic anisotropy patterns in subduction zones and are especially helpful for defining regions of uniform olivine texture as a source of seismic anisotropy in different subduction settings. The clustering analysis reveals significant heterogeneity in seismic anisotropy, approximated by olivine a-axis texture, with clusters spaced approximately 100–200 km apart around the slab edge and 200–300 km apart farther into the center of the subduction zone (Figures 7 and 8). Below 410 km in the mantle transition zone

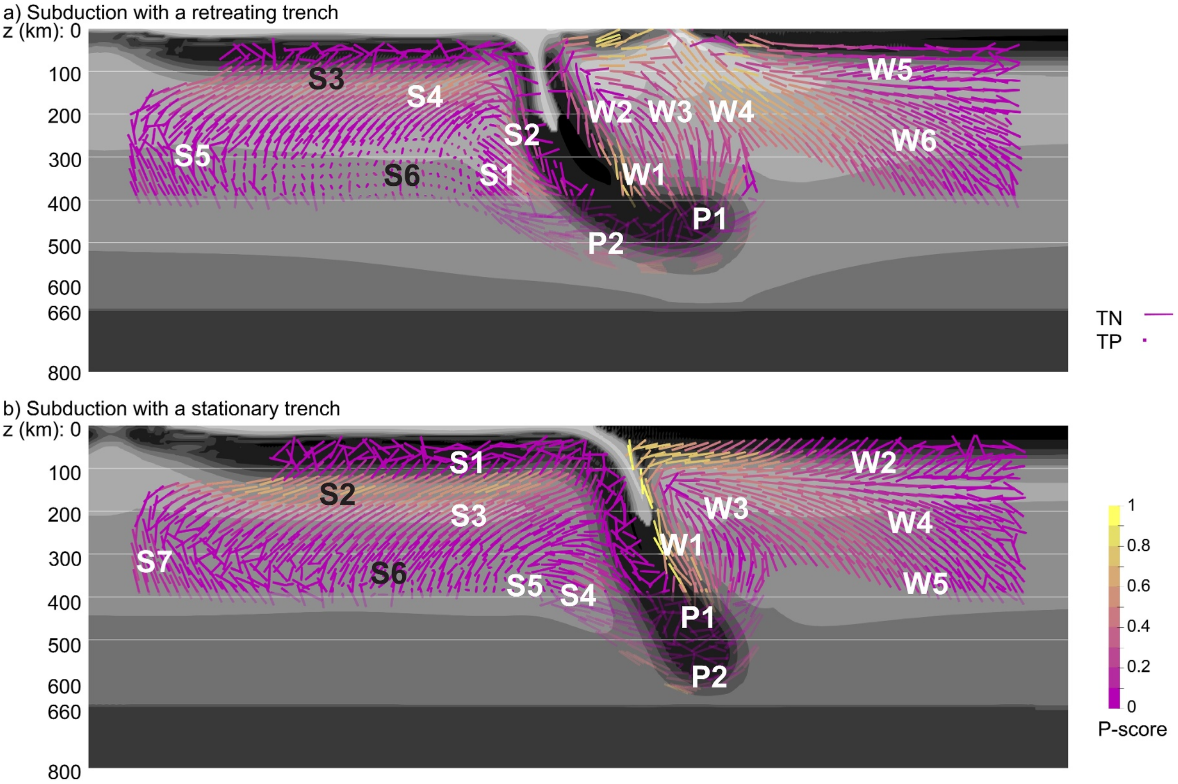

Figure 7. Mean olivine *a*-axis orientations for tracers on the center cross-section, colored by their P-scores representing the anisotropy amplitude above a background of the viscosity at the end of the model. The top panel (a) is for the retreating-trench subduction model and the bottom panel (b) is for the stationary-trench subduction model. The orientations are 3D lines such that if the line shows its full length, the orientation is trench-normal, and if the line appears as a point, the orientation is trench-parallel.

(MTZ), Mainprice et al. (1990) suggest that during the phase transition, the new phase may inherit orientations from the old phase (e.g., the olivine to spinel phase transition). They propose a method to compute the inherited CPO based on the orientation relationship between the two phases on orientations (Mainprice et al., 1990). Faccenda (2014) and Magali et al. (2024), on the other hand, implemented a simplified version of the phase transition, which assigns a random CPO to aggregates that travel into the MTZ. Our implementation of phase transition only happens in the texture prediction post-processing step for MDM and MDM + AV and does not affect the viscosity structure of the model. Although this simplified representation of the effect of phase transition on anisotropy limits our interpretation, we can still infer the relationship between CPO and CPO-induced AV for clusters that include tracers that have not crossed into the MTZ (cluster groups W and S).

4.2.1. Poloidal Flow in Subduction Zones

We identified that the most significant seismic anisotropy in the subduction model with a retreating trench is located in the mantle wedge region (W1, W3, and W4) and below the subducting plate (S3 and S4), and is oriented in a trench-normal direction (Figure 3). This is also visible in Figure 7a, where the trench-normal signals exhibit larger amplitudes (yellowish) compared to the oblique or trench-parallel signals. Such trench-normal signals have been observed in many subduction zones, for example, in the back-arc region in the Tonga subduction zone (Fischer et al., 2000) and in the Scotia Sea (Müller, 2001), and have been interpreted as poloidal flow coupled to the down-going slab. Between 300 and 400 km depth behind the slab, the trench-parallel signals from cluster S2 are well-separated from the weaker and oblique signals around them (Figure 7a). The trench-parallel fast direction in the sub-slab region has been observed up to 400 km depth, for example, in the Tongan (Foley & Long, 2011), Caribbean (Lynner & Long, 2013), and Scotian (Lynner & Long, 2013) subduction systems. In the other parts of the model, the anisotropy is much weaker and trench-oblique in different orientations.

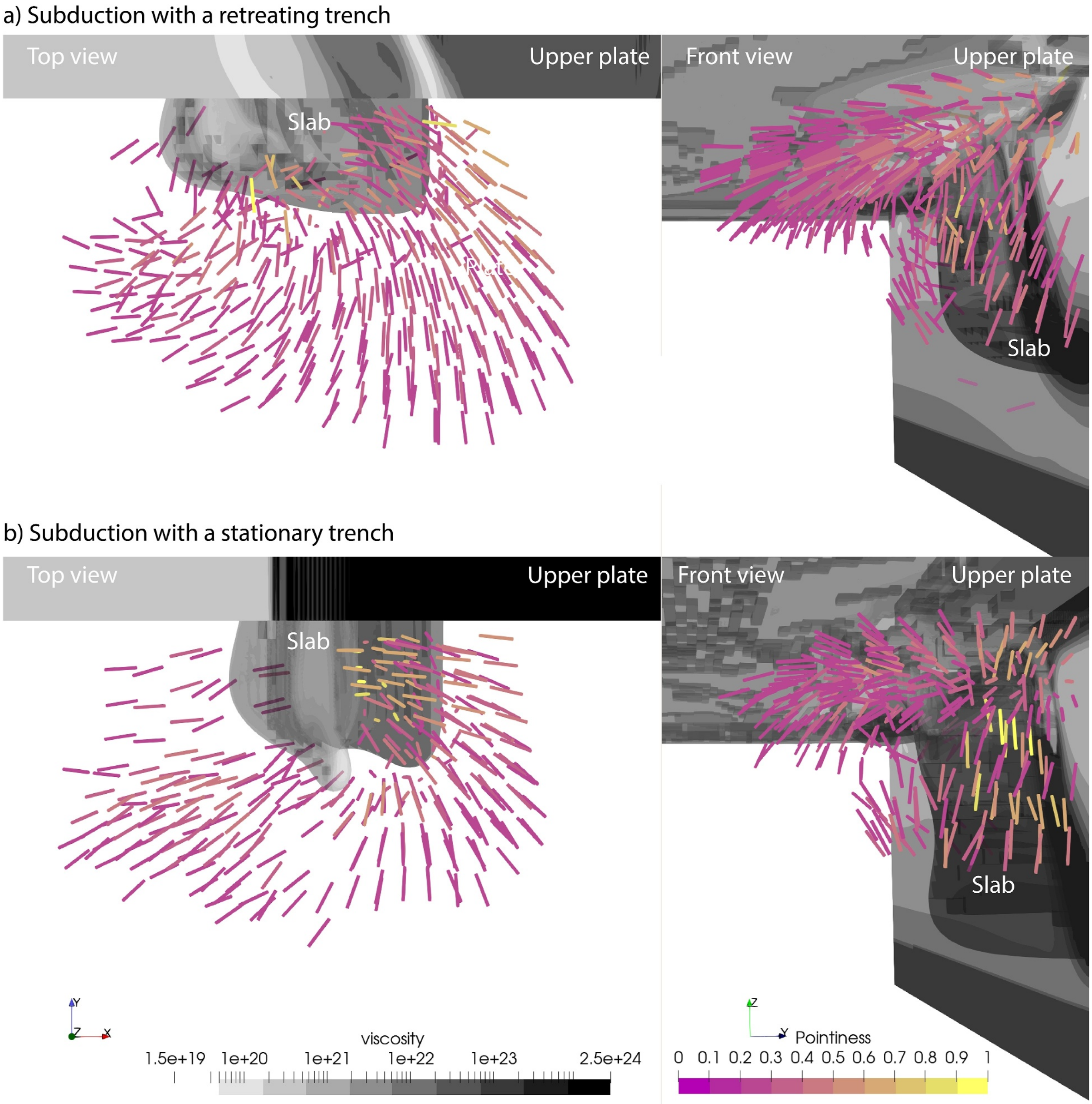

Figure 8. The same as for Figure 7, but for tracers on the slab edge of (a) in the retreating-trench subduction model and (b) in the stationary-trench subduction model.

Trench-normal orientations are also the strongest and the most widespread signals in the stationary-trench model (as for the retreating-trench model), but the locations of such orientations vary between the two models (Figure 7). In the retreating-trench model (Figure 7a), most trench-normal orientations are located below the opening back-arc basin in the mantle wedge region, while in the stationary-trench model (Figure 7b), there are relatively stronger trench-normal signals directly beneath both the subducting plate (S2 and S3) and the overriding plate (W2), and at the plate interface (W1). These differences are likely due to deformation induced by additional basal drag associated with convergence between the subducting and the overriding plates. In general, our models suggest that horizontal anisotropy is stronger in the retreating trench configuration compared to the stationary trench model, both at the center of the subduction zone and near the slab edge. This may be linked to more vigorous mantle deformation induced by trench retreat. However, greater anisotropy amplitudes have not been reported for retreating trenches. Instead, existing anisotropy studies primarily focus on the directionality of anisotropy rather than amplitude. Given that anisotropy amplitude observations from studies using different methods and resolutions are not directly comparable, designing future seismic studies specifically targeting amplitude comparisons across different subduction types could provide valuable insights.

Long's (2013) summary of seismic anisotropy orientations in the mantle wedge also shows that trench-parallel anisotropy transitioning to trench-normal orientations away from the slab occurs more often than trench-normal orientations alone. We find no strong and clear trench-parallel signal in the center of our models where tracers experience dominant poloidal flow. In the mantle wedge region, if water is present at low-temperature and high-stress conditions, several studies (Jung & Karato, 2001; Kneller et al., 2008; Long et al., 2007) suggest that the presence of B-type olivine fabric could lead to trench-parallel fast directions in seismic anisotropy. In our MDM + AV texture prediction model, different olivine fabrics and the effect of water are not included. Trench-parallel or oblique orientations might also be induced by more complex slab geometries with locally flattened sections, as in Peru (MacDougall et al., 2012). This might induce additional lateral flows both in front of and behind the slab that cannot be accounted for in our models. Apart from this, the absence of trench-parallel orientations in our model could also be related to incomplete coupling between texture evolution, anisotropic viscosity, and model dynamics. The feedback effect that would allow anisotropic viscosity to change deformation has not yet been implemented in our modeling method but could result in changes to flow that produce seismically observable rock textures.

4.2.2. Toroidal Flow in Subduction Zone

On the lateral edge of the slab, we observe a variety of anisotropy orientations due to toroidal flow around the slab edge (Figure 8). Tracers are clustered into groups that end up oriented in different oblique directions, capturing different portions of the toroidal flow around the slab edge. In the subduction model with a retreating trench, we observe a transition from trench-normal to oblique or trench-parallel orientations during the evolution of the model induced by the toroidal flow (Figure 6). This is consistent with mantle material from all directions being transported to fill the space left by the retreating trench. Such trench-parallel orientations are not observed during the evolution of the subduction zone with a stationary trench due to the lack of horizontal toroidal flow in that model, and anisotropy in this model is also weak.

Toroidal flow in subduction zones is usually observed in trench-parallel fast directions in the mantle wedge and sub-slab regions that wrap around slab edges. As in our model of a retreating subduction zone, the fast directions at the edge of the slab represent different portions of toroidal flow with a variety of orientations ranging from trench-parallel to trench-normal (Figure 8). Typical toroidal flow cells in subduction systems that are interpreted from SKS observations include, for example, the Caribbean and Scotia subduction zones (Russo & Silver, 1994), the Tonga subduction zone (Foley & Long, 2011; Yu et al., 2022), the Calabrian subduction zone (Baccheschi et al., 2024; Civello & Margheriti, 2004; Faccenna et al., 2014), and the Cascadia subduction zone (Zandt & Humphreys, 2008).

5. Conclusions

This study demonstrates the utility of time-series clustering for identifying regions of distinct olivine texture and seismic anisotropy in subduction zones. Clustering analysis can successfully identify heterogeneity in the evolution of texture and deformation stored on tracers in the subduction model and could also be applied to other time-series data obtained in geodynamic models. Our comparison of D-Rex, MDM, and MDM + AV texture prediction methods indicates that the regions most affected by AV are those that have more developed and point-like olivine textures. In these, the pointiness scores from MDM + AV textures are similar to or even greater than those from D-Rex. The heterogeneity in olivine a-axis orientations revealed by the clustering analysis is comparable to scale and orientation to seismic anisotropy in subduction zones. In particular, we observe predominantly trench-normal orientations in the mantle wedge and sub-slab regions, with the toroidal flow around slab edges producing a variety of trench-oblique orientations. The textures are, in general, stronger and more developed in the retreating trench model than in the stationary one. Our results reveal heterogeneities in olivine textures in subduction models both horizontally and across vertical depths. Our models provide good constraints on the spatial and temporal variability of mantle textures in subduction zones, which in the future can be useful for comparison with regional, depth-sensitive seismic anisotropy studies. This study underscores the complex interplay between mantle flow, olivine texture, and seismic anisotropy, which can vary significantly depending on trench kinematics and the inclusion of AV in texture models but can be characterized using clustering methods.

Data Availability Statement

Parameter files, Matlab, and Python scripts for olivine texture computations and clustering analysis are available through Zenodo (Wang, 2025).

Acknowledgments
This research was supported by the Research Council of Norway's projects 314742 (ANIMA) and 332523 (Center for Planetary Habitability). We thank the Norwegian Research Infrastructure Service (NRIS/Sigma2) for providing the computational resources via projects NN9283k and NN9894k. We also thank the Computational Infrastructure for Geodynamics, funded by the National Science Foundation under awards EAR-0949446 and EAR-1550901, for supporting the development of ASPECT.

References

Baccheschi, P., Confal, J. M., & Pondrelli, S. (2024). Splitting intensity tomography to image depth-dependent seismic anisotropy patterns beneath the Italian Peninsula and surrounding regions. *Earth and Planetary Science Letters*, *646*, 119005. https://doi.org/10.1016/j.epsl.2024.119005

Bangerth, W., Dannberg, J., Fraters, M., Gassmoeller, R., Glerum, A., Heister, T., et al. (2022). ASPECT v2.4.0 [Computer software]. *Zenodo*. https://doi.org/10.5281/zenodo.6903424

Becker, T. W., Chevrot, S., Schulte-Pelkum, V., & Blackman, D. K. (2006). Statistical properties of seismic anisotropy predicted by upper mantle geodynamic models. *Journal of Geophysical Research*, *111*(B8). https://doi.org/10.1029/2005JB004095

Behr, W. M., Holt, A. F., Becker, T. W., & Faccenna, C. (2022). The effects of plate interface rheology on subduction kinematics and dynamics. *Geophysical Journal International*, *230*(2), 796–812. https://doi.org/10.1093/gji/ggac075

Boneh, Y., & Skemer, P. (2014). The effect of deformation history on the evolution of olivine CPO. *Earth and Planetary Science Letters*, *406*, 213–222. https://doi.org/10.1016/J.EPSL.2014.09.018

Civello, S., & Margheriti, L. (2004). Toroidal mantle flow around the Calabrian slab (Italy) from SKS splitting. *Geophysical Research Letters*, *31*(10), 2004GL019607. https://doi.org/10.1029/2004GL019607

Crameri, F., Conrad, C. P., Montési, L., & Lithgow-Bertelloni, C. R. (2019). The dynamic life of an oceanic plate. *Tectonophysics*, *760*, 107–135. https://doi.org/10.1016/j.tecto.2018.03.016

Davies, D. L., & Bouldin, D. W. (1979). A cluster separation measure. *IEEE Transactions on Pattern Analysis and Machine Intelligence*, *PAMI-1*(2), 224–227. https://doi.org/10.1109/TPAMI.1979.4766909

Di Leo, J. F., Walker, A. M., Li, Z.-H., Wookey, J., Ribe, N. M., Kendall, J.-M., & Tommasi, A. (2014). Development of texture and seismic anisotropy during the onset of subduction. *Geochemistry, Geophysics, Geosystems*, *15*(1), 192–212. https://doi.org/10.1002/2013GC005032

Duarte, J. C., Schellart, W. P., & Cruden, A. R. (2013). Three-dimensional dynamic laboratory models of subduction with an overriding plate and variable interplate rheology. *Geophysical Journal International*, *195*(1), 47–66. https://doi.org/10.1093/gji/ggt257

Faccenda, M. (2014). Mid mantle seismic anisotropy around subduction zones. *Physics of the Earth and Planetary Interiors*, *227*, 1–19. https://doi.org/10.1016/j.pepi.2013.11.015

Faccenda, M., & Capitanio, F. A. (2012). Development of mantle seismic anisotropy during subduction-induced 3-D flow: Mantle seismic anisotropy in 3-D flow. *Geophysical Research Letters*, *39*(11). https://doi.org/10.1029/2012GL051988

Faccenda, M., & Capitanio, F. A. (2013). Seismic anisotropy around subduction zones: Insights from three-dimensional modeling of upper mantle deformation and SKS splitting calculations. *Geochemistry, Geophysics, Geosystems*, *14*(1), 243–262. https://doi.org/10.1002/ggge.20055

Faccenna, C., Becker, T. W., Auer, L., Billi, A., Boschi, L., Brun, J. P., et al. (2014). Mantle dynamics in the Mediterranean: Mediterranean dynamic. *Reviews of Geophysics*, *52*(3), 283–332. https://doi.org/10.1002/2013RG000444

Fischer, K. M., Parmentier, E. M., Stine, A. R., & Wolf, E. R. (2000). Modeling anisotropy and plate-driven flow in the Tonga subduction zone back arc. *Journal of Geophysical Research*, *105*(B7), 16181–16191. https://doi.org/10.1029/1999JB900441

Foley, B. J., & Long, M. D. (2011). Upper and mid-mantle anisotropy beneath the Tonga slab: Anisotropy beneath Tonga slab. *Geophysical Research Letters*, *38*(2). https://doi.org/10.1029/2010GL046021

Fraters, M. R. T., & Billen, M. I. (2021). On the implementation and usability of crystal preferred orientation evolution in geodynamic modeling. *Geochemistry, Geophysics, Geosystems*, *22*(10). https://doi.org/10.1029/2021GC009846

Funiciello, F., Moroni, M., Piromallo, C., Faccenna, C., Cenedese, A., & Bui, H. A. (2006). Mapping mantle flow during retreating subduction: Laboratory models analyzed by feature tracking. *Journal of Geophysical Research*, *111*(B3), 2005JB003792. https://doi.org/10.1029/2005JB003792

Funiciello, F., Morra, G., Regenauer-Lieb, K., & Giardini, D. (2003). Dynamics of retreating slabs: 1. Insights from two-dimensional numerical experiments. *Journal of Geophysical Research*, *108*(B4). https://doi.org/10.1029/2001JB000898

Gea, P. J., de Mancilla, F. L., Negredo, A. M., & van Hunen, J. (2024). Overriding Plate Thickness as a Controlling Factor for Trench Retreat Rates in Narrow Subduction Zones. *Geochemistry, Geophysics, Geosystems*, *25*(2), e2023GC011345. https://doi.org/10.1029/2023GC011345

Guillaume, B., Funiciello, F., & Faccenna, C. (2021). Interplays between mantle flow and slab pull at subduction zones in 3D. *Journal of Geophysical Research: Solid Earth*, *126*(5), e2020JB021574. https://doi.org/10.1029/2020JB021574

Hansen, L. N., Conrad, C. P., Boneh, Y., Skemer, P., Warren, J. M., & Kohlstedt, D. L. (2016). Viscous anisotropy of textured olivine aggregates: 2. Micromechanical model. *Journal of Geophysical Research: Solid Earth*, *121*(10), 7137–7160. https://doi.org/10.1002/2016JB013240

Hansen, L. N., Warren, J. M., Zimmerman, M. E., & Kohlstedt, D. L. (2016). Viscous anisotropy of textured olivine aggregates, Part 1: Measurement of the magnitude and evolution of anisotropy. *Earth and Planetary Science Letters*, *445*, 92–103. https://doi.org/10.1016/j.epsl.2016.04.008

Hansen, L. N., Zimmerman, M. E., & Kohlstedt, D. L. (2012). Laboratory measurements of the viscous anisotropy of olivine aggregates. *Nature*, *492*(7429), 415–418. https://doi.org/10.1038/nature11671

Hartigan, J. A., & Wong, M. A. (1979). Algorithm AS 136: A K-means clustering algorithm. *Journal of the Royal Statistical Society. Series C (Applied Statistics)*, *28*(1), 100–108. https://doi.org/10.2307/2346830

Heister, T., Dannberg, J., Gassmöller, R., & Bangerth, W. (2017). High accuracy mantle convection simulation through modern numerical methods—II: Realistic models and problems. *Geophysical Journal International*, *210*(2), 833–851. https://doi.org/10.1093/gji/ggx195

Hill, R. (1948). A theory of the yielding and plastic flow of anisotropic metals. *Proceedings of the Royal Society of London. Series A. Mathematical and Physical Sciences*, *193*(1033), 281–297. https://doi.org/10.1098/rspa.1948.0045

Jadamec, M. A., & Billen, M. I. (2010). Reconciling surface plate motions with rapid three-dimensional mantle flow around a slab edge. *Nature*, *465*(7296), 338–341. https://doi.org/10.1038/nature09053

Jung, H., & Karato, S. (2001). Water-induced fabric transitions in olivine. *Science*, *293*(5534), 1460–1463. https://doi.org/10.1126/SCIENCE.1062235

Kaminski, É., Ribe, N. M., & Browaeys, J. T. (2004). D-Rex, a program for calculation of seismic anisotropy due to crystal lattice preferred orientation in the convective upper mantle. *Geophysical Journal International*, *158*(2), 744–752. https://doi.org/10.1111/j.1365-246X.2004.02308.x

Kanungo, T., Mount, D. M., Netanyahu, N. S., Piatko, C. D., Silverman, R., & Wu, A. Y. (2002). An efficient k-means clustering algorithm: Analysis and implementation. *IEEE Transactions on Pattern Analysis and Machine Intelligence*, *24*(7), 881–892. https://doi.org/10.1109/TPAMI.2002.1017616

Karato, S., Jung, H., Katayama, I., & Skemer, P. (2008). Geodynamic significance of seismic anisotropy of the upper mantle: New insights from laboratory studies. *Annual Review of Earth and Planetary Sciences*, *36*(1), 59–95. https://doi.org/10.1146/annurev.earth.36.031207.124120

Király, Á., Capitanio, F. A., Funiciello, F., & Faccenna, C. (2017). Subduction induced mantle flow: Length-scales and orientation of the toroidal cell. *Earth and Planetary Science Letters*, *479*, 284–297. https://doi.org/10.1016/j.epsl.2017.09.017

Király, Á., Conrad, C. P., & Hansen, L. N. (2020). Evolving viscous anisotropy in the upper mantle and its geodynamic implications. *Geochemistry, Geophysics, Geosystems*, *21*(10). https://doi.org/10.1029/2020GC009159

Kneller, E. A., Long, M. D., & van Keken, P. E. (2008). Olivine fabric transitions and shear wave anisotropy in the Ryukyu subduction system. *Earth and Planetary Science Letters*, *268*(3), 268–282. https://doi.org/10.1016/j.epsl.2008.01.004

Kronbichler, M., Heister, T., & Bangerth, W. (2012). High accuracy mantle convection simulation through modern numerical methods. *Geophysical Journal International*, *191*(1), 12–29. https://doi.org/10.1111/j.1365-246X.2012.05609.x

Long, M. D. (2013). Constraints on subduction geodynamics from seismic anisotropy. *Reviews of Geophysics*, *51*(1), 76–112. https://doi.org/10.1002/rog.20008

Long, M. D., & Becker, T. W. (2010). Mantle dynamics and seismic anisotropy. *Earth and Planetary Science Letters*, *297*(3), 341–354. https://doi.org/10.1016/j.epsl.2010.06.036

Long, M. D., Hager, B. H., de Hoop, M. V., & van der Hilst, R. D. (2007). Two-dimensional modelling of subduction zone anisotropy with application to southwestern Japan. *Geophysical Journal International*, *170*(2), 839–856. https://doi.org/10.1111/j.1365-246X.2007.03464.x

Long, M. D., & Wirth, E. A. (2013). Mantle flow in subduction systems: The mantle wedge flow field and implications for wedge processes. *Journal of Geophysical Research: Solid Earth*, *118*(2), 583–606. https://doi.org/10.1002/jgrb.50063

Lynner, C., & Beck, S. L. (2020). Subduction dynamics and structural controls on shear wave splitting along the South American convergent margin. *Journal of South American Earth Sciences*, *104*, 102824. https://doi.org/10.1016/j.jsames.2020.102824

Lynner, C., & Long, M. D. (2013). Sub-slab seismic anisotropy and mantle flow beneath the Caribbean and Scotia subduction zones: Effects of slab morphology and kinematics. *Earth and Planetary Science Letters*, *361*, 367–378. https://doi.org/10.1016/j.epsl.2012.11.007

Lynner, C., & Long, M. D. (2014). Testing models of sub-slab anisotropy using a global compilation of source-side shear wave splitting data. *Journal of Geophysical Research: Solid Earth*, *119*(9), 7226–7244. https://doi.org/10.1002/2014JB010983

MacDougall, J. G., Fischer, K. M., & Anderson, M. L. (2012). Seismic anisotropy above and below the subducting Nazca lithosphere in southern South America. *Journal of Geophysical Research*, *117*(B12). https://doi.org/10.1029/2012JB009538

Magali, J. K., Ledoux, E. E., Thomas, C., Capdeville, Y., & Merkel, S. (2024). Pressure-dependent large-scale seismic anisotropy induced by non-Newtonian mantle flow. *Geophysical Journal International*, *238*(1), 400–419. https://doi.org/10.1093/gji/ggae165

Magni, V., Király, Á., Lynner, C., Avila, P., & Gill, J. (2024). Mantle flow in subduction systems and its effects on surface tectonics and magmatism. *Nature Reviews Earth & Environment*, 1–16. https://doi.org/10.1038/s43017-024-00612-3

Mainprice, D., Humbert, M., & Wagner, F. (1990). Phase transformations and inherited lattice preferred orientations: implications for seismic properties. *Tectonophysics*, *180*(2–4), 213–228. https://doi.org/10.1016/0040-1951(90)90309-v

Müller, C. (2001). Upper mantle seismic anisotropy beneath Antarctica and the Scotia Sea region. *Geophysical Journal International*, *147*(1), 105–122. https://doi.org/10.1046/j.1365-246X.2001.00517.x

Peng, C.-C., Kuo, B.-Y., & Tan, E. (2021). Dual structure of poloidal and toroidal flow under the Cocos subduction zone. *Earth and Planetary Science Letters*, *565*, 116911. https://doi.org/10.1016/j.epsl.2021.116911

Piromallo, C., Becker, T. W., Funiciello, F., & Faccenna, C. (2006). Three-dimensional instantaneous mantle flow induced by subduction. *Geophysical Research Letters*, *33*(8), 2005GL025390. https://doi.org/10.1029/2005GL025390

Rappisi, F., VanderBeek, B. P., Faccenda, M., Morelli, A., & Molinari, I. (2022). Slab Geometry and Upper Mantle Flow Patterns in the Central Mediterranean From 3D Anisotropic P-Wave Tomography. *Journal of Geophysical Research: Solid Earth*, *127*(5), e2021JB023488. https://doi.org/10.1029/2021JB023488

Ribe, N. M. (1989). Seismic anisotropy and mantle flow. *Journal of Geophysical Research*, *94*(B4), 4213–4223. https://doi.org/10.1029/JB094iB04p04213

Rousseeuw, P. J. (1987). Silhouettes: A graphical aid to the interpretation and validation of cluster analysis. *Journal of Computational and Applied Mathematics*, *20*, 53–65. https://doi.org/10.1016/0377-0427(87)90125-7

Royden, L. H., & Husson, L. (2006). Trench motion, slab geometry and viscous stresses in subduction systems. *Geophysical Journal International*, *167*(2), 881–905. https://doi.org/10.1111/j.1365-246X.2006.03079.x

Russo, R. M., & Silver, P. G. (1994). Trench-parallel flow beneath the Nazca plate from seismic anisotropy. *Science*, *263*(5150), 1105–1111. https://doi.org/10.1126/science.263.5150.1105

Schellart, W. P., Freeman, J., Stegman, D. R., Moresi, L., & May, D. (2007). Evolution and diversity of subduction zones controlled by slab width. *Nature*, *446*(7133), 308–311. https://doi.org/10.1038/nature05615

Schellart, W. P., & Moresi, L. (2013). A new driving mechanism for backarc extension and backarc shortening through slab sinking induced toroidal and poloidal mantle flow: Results from dynamic subduction models with an overriding plate. *Journal of Geophysical Research: Solid Earth*, *118*(6), 3221–3248. https://doi.org/10.1002/jgrb.50173

Signorelli, J., Hassani, R., Tommasi, A., & Mameri, L. (2021). An effective parameterization of texture-induced viscous anisotropy in orthotropic materials with application for modeling geodynamical flows. *Journal of Theoretical, Computational and Applied Mechanics*, *6737*. https://doi.org/10.46298/jtcam.6737

Skemer, P., & Hansen, L. (2016). Inferring upper-mantle flow from seismic anisotropy: An experimental perspective. *Tectonophysics*, *668*, 1–14. https://doi.org/10.1016/J.TECTO.2015.12.003

Skemer, P., Katayama, I., Jiang, Z., & Karato, S. (2005). The misorientation index: Development of a new method for calculating the strength of lattice-preferred orientation. *Tectonophysics*, *411*(1–4), 157–167. https://doi.org/10.1016/j.tecto.2005.08.023

Strak, V., & Schellart, W. P. (2014). Evolution of 3-D subduction-induced mantle flow around lateral slab edges in analogue models of free subduction analysed by stereoscopic particle image velocimetry technique. *Earth and Planetary Science Letters*, *403*, 368–379. https://doi.org/10.1016/j.epsl.2014.07.007

Tommasi, A., Mainprice, D., Canova, G., & Chastel, Y. (2000). Viscoplastic self-consistent and equilibrium-based modeling of olivine lattice preferred orientations: Implications for the upper mantle seismic anisotropy. *Journal of Geophysical Research*, *105*(B4), 7893–7908. https://doi.org/10.1029/1999JB900411

Turino, V., & Holt, A. F. (2024). Spatio-temporal variability in slab temperature within dynamic 3-D subduction models. *Geophysical Journal International*, *236*(3), 1484–1498. https://doi.org/10.1093/gji/ggad489

VanderBeek, B. P., & Faccenda, M. (2021). Imaging upper mantle anisotropy with teleseismic P-wave delays: Insights from tomographic reconstructions of subduction simulations. *Geophysical Journal International*, *225*(3), 2097–2119. https://doi.org/10.1093/gji/ggab081

Vollmer, F. W. (1990). An application of eigenvalue methods to structural domain analysis. *Geological Society of America Bulletin*, *102*(6), 786–791. https://doi.org/10.1130/0016-7606(1990)102<0786:AAOEMT>2.3.CO;2

Walpole, J., Wookey, J., Kendall, J.-M., & Masters, T.-G. (2017). Seismic anisotropy and mantle flow below subducting slabs. *Earth and Planetary Science Letters*, *465*, 155–167. https://doi.org/10.1016/j.epsl.2017.02.023

Wang, Y. (2025). Scripts to reproduce the results in manuscript2 [Computer software]. *Zenodo*. https://doi.org/10.5281/zenodo.15388150

Wang, Y., Király, A., Conrad, C., Hansen, L., & Fraters, M. (2024). The importance of anisotropic viscosity in numerical models, for olivine textures in shear and subduction deformations. *Τεκτονικα*, *2*(1). Article 1. https://doi.org/10.55575/tektonika2024.2.1.67

Warren Liao, T. (2005). Clustering of time series data—A survey. *Pattern Recognition*, *38*(11), 1857–1874. https://doi.org/10.1016/j.patcog.2005.01.025

Yu, Z., Zhao, D., & Li, J. (2022). Structure and dynamics of the Tonga subduction zone: New insight from P-wave anisotropic tomography. *Earth and Planetary Science Letters*, *598*, 117844. https://doi.org/10.1016/j.epsl.2022.117844

Zandt, G., & Humphreys, E. (2008). Toroidal mantle flow through the western U.S. slab window. *Geology*, *36*(4), 295–298. https://doi.org/10.1130/G24611A.1

Zhu, H., Li, X., Yang, J., Stern, R. J., & Lumley, D. E. (2020). Poloidal- and toroidal-mode mantle flows underneath the Cascadia subduction zone. *Geophysical Research Letters*, *47*(14), e2020GL087530. https://doi.org/10.1029/2020GL087530